Improving powertrain efficiency through torque modulation techniques in single and dual motor electric vehicles

Transportation Engineering 18 (2024) 100289

Contents lists available at ScienceDirect

Transportation Engineering

journal homepage: www.sciencedirect.com/journal/transportation-engineering

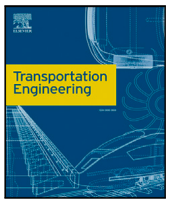

Full length article

Improving powertrain efficiency through torque modulation techniques in single and dual motor electric vehicles

Y. Xu [a,b,*], P. Ingelström [c], A. Kersten [d], A. Andersson [e], S. Klacar [e], S. George [e], D. Sedarsky [b]

[a] Zeekr Technology Europe AB, Göteborg, Sweden
[b] Chalmers University of Technology, Division of Energy Conversion and Propulsion Systems, Mechanics and Maritime Sciences, Göteborg, Sweden
[c] RISE Research Institutes of Sweden, Göteborg, Sweden
[d] University West, Department of Electrical Engineering, Trollhättan, Sweden
[e] Infimotion Technology Europe AB, Göteborg, Sweden

ARTICLE INFO

Keywords:
Battery Electric Vehicle (BEV)
Driver comfort
Energy efficiency
Powertrain
Torque modulation

ABSTRACT

Battery Electric Vehicles (BEVs) typically experience reduced powertrain energy efficiency under low-torque operating conditions. This issue can be mitigated by torque modulation, i.e., alternating driver torque demand between zero and an appropriate value. This paper aims to maximize the efficiency improvement of torque modulation and investigate its potential in two powertrain topologies: single and dual motor powertrains. To this end, optimal modulation strategies are proposed for both powertrains, considering overall powertrain energy losses and specific powertrain characteristics. Additionally, the adverse impact on driver comfort and powertrain durability due to the pulsating torque is examined. The results suggest that the proposed optimal modulation strategies can enhance powertrain efficiency while maintaining acceptable levels of driver comfort and powertrain durability. In addition, complementary modulation and torque distribution can be applied in the dual motor powertrain to provide further energy-saving potential and reduced impact on driver comfort.

1. Introduction

With the global emphasis on sustainable transportation and environmental conservation, the automotive industry is experiencing a significant shift towards electrified mobility solutions. Battery Electric Vehicles (BEVs) lead this transition for passenger vehicles, offering a viable alternative to traditional Internal Combustion Engine Vehicles (ICEVs) in terms of reduced greenhouse gas emissions [1,2], independence from fossil fuels, and enhanced NVH performance [3]. Nevertheless, a number of challenges persist such as constrained driving range [4], battery cost [5], and underdeveloped charging infrastructure [6], which have collectively hindered the adoption of BEVs. Thus, enhancing the energy efficiency of the BEV powertrain remains an important aspect to address these concerns. As the key BEV powertrain loss contributor, a state-of-the-art electric motor can reach up to 97% peak efficiency [7,8]. However, most traction electric motors such as Induction Motor (IM), Permanent Magnet Synchronous Motor (PMSM) and Synchronous Reluctance Motor (SynRM) exhibit non-uniformly distributed efficiency across the speed-torque operating range, despite having varying high-efficiency operating regions [9]. This results in differences in energy efficiency across various driving conditions for vehicles, creating challenges in effectively utilizing the optimal efficiency operating range [10]. In general, electric motors suffer from decreased efficiency at both low and high torque operating areas [11,12]. To avoid the low energy efficiency in low torque operations, the torque demand can be modulated as a varying signal, oscillating between different torque levels at a high frequency, while the average output torque remains the same as the original torque demand. With such torque modulation technique, the inefficient operating zones in the low torque range can be avoided.

Several studies have investigated the effectiveness of torque modulation with specific modulation strategies. One example is the "Dynamic Motor Drive" (referred to as the DMD strategy) proposed by Tula Technology in [13,14]. Under low torque operating conditions, the DMD strategy alternates the motor torque demand between zero and peak efficiency torque levels. Consequently, the pulsating torque ensures the motor operates at its highest efficiency at the corresponding speed, bypassing the inefficient operating zones in the low torque range. With the DMD strategy, it is reported that approximately a 2.5% reduction of energy consumption over the Worldwide Harmonized Light Vehicles Test Cycle (WLTC) drive cycle can be achieved for a Chevrolet Bolt vehicle equipped with a 150-kW SynRM [15]. In [16],

* Corresponding author at: Chalmers University of Technology, Division of Energy Conversion and Propulsion Systems, Mechanics and Maritime Sciences, Göteborg, Sweden.
E-mail address: yuxu@chalmers.se (Y. Xu).

https://doi.org/10.1016/j.treng.2024.100289
Received 25 March 2024; Received in revised form 8 October 2024; Accepted 1 November 2024
Available online 10 November 2024

the energy-saving potential of the torque modulation technique with DMD strategy is further examined for powertrains equipped with an Electrically Excited Synchronous Motor (EESM) and an Interior Permanent Magnet Synchronous Motor (IPMSM), showing a WLTC drive-cycle energy consumption reduction of 2% and 0.4%, respectively.

Although the DMD strategy demonstrates promising improvements in powertrain efficiency, it is derived based solely on the optimal efficiency torque of the inverter and motor while neglecting the energy losses from the battery and transmission. This leads to a suboptimal solution from an overall powertrain system perspective. High-amplitude on-torque during modulation can induce peak battery currents, resulting in increased battery losses [17,18], while transmissions typically achieve higher efficiency at higher torque operations [19]. Therefore, there is a need for a torque modulation strategy that balances efficiency gains and losses among different powertrain components to maximize overall powertrain efficiency.

On the other hand, dual motor powertrains are becoming a promising alternative to single motor BEV powertrains in the current market [20], though a vehicle with a dual motor powertrain might exhibit slightly higher energy consumption compared to its single motor powertrain variant [21]. As the most dominant type of dual motor powertrain in the current BEV market, the front- and rear-axle independently driven powertrain offers superior All-Wheel-Drive (AWD) capability, fault-tolerance, and torque distribution freedom [22,23]. This is showcased by most commercial BEVs such as the Polestar 2, Tesla Model Y, and Volvo C40 Recharge, offering such dual motor powertrains alongside their single motor configurations [24]. Specifically, distributing the torque demand between the motors can mitigate the inefficient operation at high torque demand situations [25–27], while the most efficient operating strategy is to have only one motor delivering the torque for low torque demand situations [28], which sacrifices the AWD capability. By implementing torque modulation in dual motor powertrains, the torque distribution capability can be utilized in low torque demand situations, allowing both motors to operate under torque modulation simultaneously. This may offer notable advantages in energy efficiency improvement as the benefits from torque modulation become more pronounced when torque demand decreases by sharing it between the two motors. However, the dual motor powertrain's higher degree of operational freedom necessitates careful consideration of overall powertrain losses when optimizing the torque modulation strategy. Since both motors can operate under high-amplitude on-torque simultaneously and lead to high superimposed battery currents and corresponding losses.

Torque modulation can degrade driver comfort and the durability of powertrain components due to resultant pulsating motor torque output and excessive load cycle variations [19]. Although increasing the torque modulation frequency in a single motor powertrain can lessen the impact on driver comfort to a certain extent, a high modulation frequency can also lead to greater transient energy loss [15]. It is plausible that the impact on driver comfort could further be reduced by modulating the torque demand between the two motors complementarily, rather than increasing the torque modulation frequency. However, few studies have looked into the application of the torque modulation technique within dual motor powertrains. Additionally, the impact of pulsating torque on powertrain component durability has not been explored.

This paper aims to address the aforementioned gaps by developing a torque modulation strategy that balances efficiency gains and losses among different powertrain components, maximizing overall powertrain efficiency. Additionally, the potential of applying torque modulation to dual motor powertrains is investigated and compared with single motor powertrains in terms of powertrain efficiency and driver comfort improvement. Furthermore, the impact of the torque modulation technique on powertrain component durability is analyzed, considering the effects of pulsating motor torque output and varying load cycles. The study offers practical solutions for both the software implementation of torque modulation techniques and the integration of powertrain topology design to enhance overall powertrain efficiency. The paper is organized as follows: Details regarding the configurations and modeling of the examined powertrains are provided in Section 2. Operating principles and limits of the torque modulation technique concerning the current controller are explored in Section 3. In Section 4, the optimization problem is formulated and the optimal modulation strategies for both single and dual motor powertrains are presented. Section 5 assesses the driver comfort, while Section 6 elaborates on the improvements in energy efficiency. Section 7 shows the impact of torque modulation on powertrain durability and conclusions are summarized in Section 8.

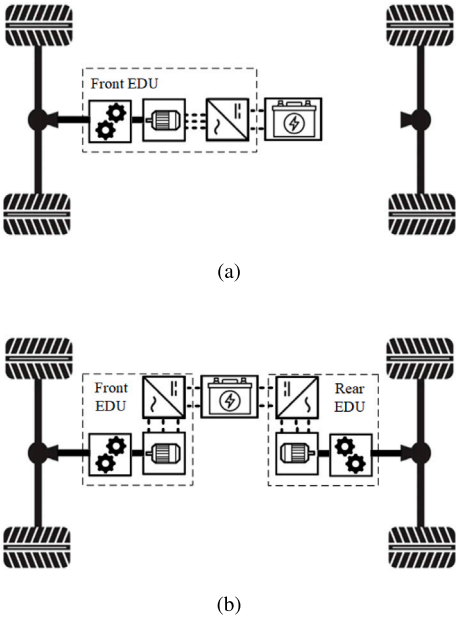

Fig. 1. Powertrain configurations: (a) Single motor powertrain and (b) dual motor powertrain.

2. System and modeling

2.1. Powertrain configuration

The configurations of the single and dual motor powertrains investigated in this paper are depicted in Fig. 1. Both powertrains are supplied by a high-voltage battery pack. The single motor powertrain is equipped with only one Electric Drive Unit (EDU) containing an inverter, an IPMSM, and a single-speed transmission to drive the front axle. Similarly, the dual motor powertrain has two sets of identical EDUs placed in the front and rear axle, respectively.

2.2. Battery

The battery equivalent electric circuit model generally consists of the open circuit voltage, V_{oc}, and the internal resistance, R_0. In addition, the dynamic and transient behavior can be more accurately modeled by incorporating one or more Thevenin ('RC') branches in the circuit which captures the main capacitive effects of the battery behavior [29,30]. In this paper a first-order RC equivalent circuit model is utilized, as shown in Fig. 2, to represent the battery's operation, which is predominantly influenced by pulsating loads induced through torque modulation.

Fig. 3 presents the identified battery cell parameters in reference to the State of Charge (SoC) from the testing at 25 °C. Subsequently, the battery pack is scaled from the individual cell configuration, adopting a setup of two parallel cells for every 93 cells connected in series (93s2p).

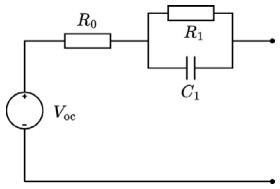

Fig. 2. First-order RC equivalent circuit battery model.

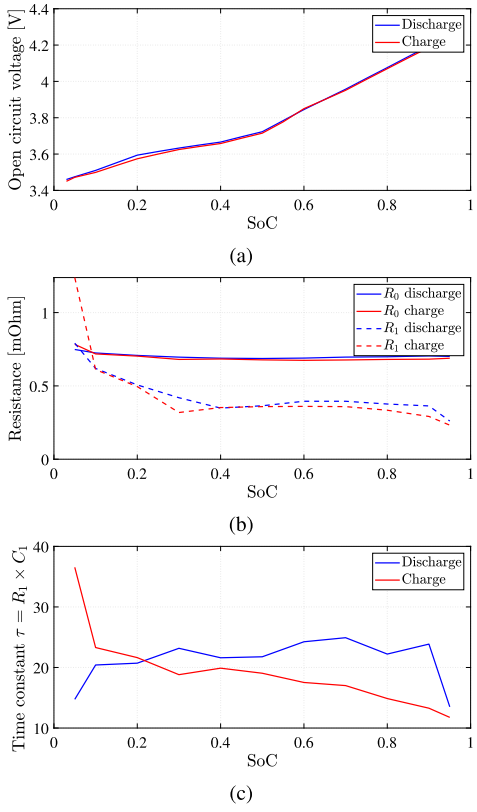

Fig. 3. Identified parameters of first-order RC equivalent circuit model of a single battery cell relative to the SoC: (a) Open circuit voltage, V_{oc}, (b) series resistance, R_0, and (c) RC branch time constant $R_1 x C_1$.

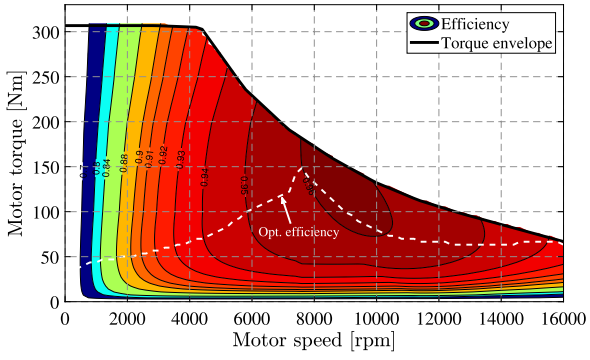

Fig. 4. Combined on-load efficiency map (propulsion side) of inverter and motor assembly at 400 V DC link voltage, V_{DC}, and 10 kHz inverter switching frequency, f_{sw}.

2.3. Inverter and motor

This study incorporates an IGBT-based three-phase inverter and a 150 kW IPMSM. Fig. 4 shows the combined efficiency characteristics of the inverter and motor assembly for the torque-speed range. Under no-load conditions (free-spinning), the back Electromotive Force (EMF) exceeds the DC voltage limit at 11 000 rpm, indicating that the inverter can be switched off only at speeds below this threshold with zero torque demand. Considering the DC voltage fluctuations arising from SoC variation during the vehicle operation, the inverter switch-off speed threshold is conservatively set at 10 200 rpm which corresponds to the minimum anticipated battery voltage of 350 V. In addition, the intermittent activation of the inverter substantially reduces iron losses within the motor when compared to the on-load condition, due to the reduced magnetic field harmonics induced by inverter switching events, as shown in Fig. 5.

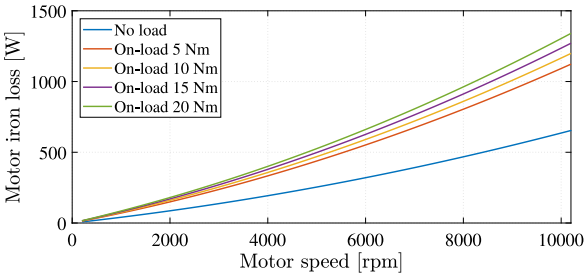

Fig. 5. Motor iron losses under no-load and on-load conditions.

Table 1
Vehicle parameters.

Parameter	Symbol	Value	Unit
Vehicle mass	m	2640	kg
Vehicle drag coefficient	C_d	0.372	–
Vehicle frontal area	A	2.8	m^2
Tire rolling radius	R_r	377	mm
Tire rolling resistance coefficient	C_r	0.01	–

2.4. Transmission

This study utilizes a two-stage single-speed transmission featuring a reduction ratio of 11.56. The transmission is subject to both load-dependent losses and no-load losses including windage effects [31]. The precision in quantifying transmission losses across various operational conditions is crucial due to the frequent transitions between on-load and no-load states required for the torque modulation approach. To this end, a detailed mapping of transmission losses and efficiency relative to the motor speed and torque is implemented, as illustrated in Fig. 6.

In addition, the transmission is considered as a non-rigid component, with torsional stiffness and damping calculated from the component's geometry. The included torsional connections are modeled as shown in Fig. 7.

2.5. Vehicle longitudinal dynamics

The resistive force on the moving vehicle consists of four terms: gradient resistance, aerodynamic resistance, tire rolling resistance, and acceleration contribution. These resistance terms are balanced with the torque demand in reference to the wheels as

$$\overbrace{\frac{T_w}{R_r}}^{\text{Tract. force}} = \overbrace{mg\sin(\theta)}^{\text{Gradient res.}} + \overbrace{\frac{1}{2}\rho_{air}C_d A v^2}^{\text{Aerodyn. drag}} + \overbrace{C_r mg\cos(\theta)}^{\text{Rolling res.}} + \overbrace{m\dot{v}}^{\text{Acc. force}} \quad (1)$$

where T_w is the vehicle torque demand in reference to the wheels, g is the gravitational acceleration, θ is the road gradient, ρ_{air} is the air density, and v is the vehicle speed. The main parameters for the investigated vehicle are listed in Table 1.

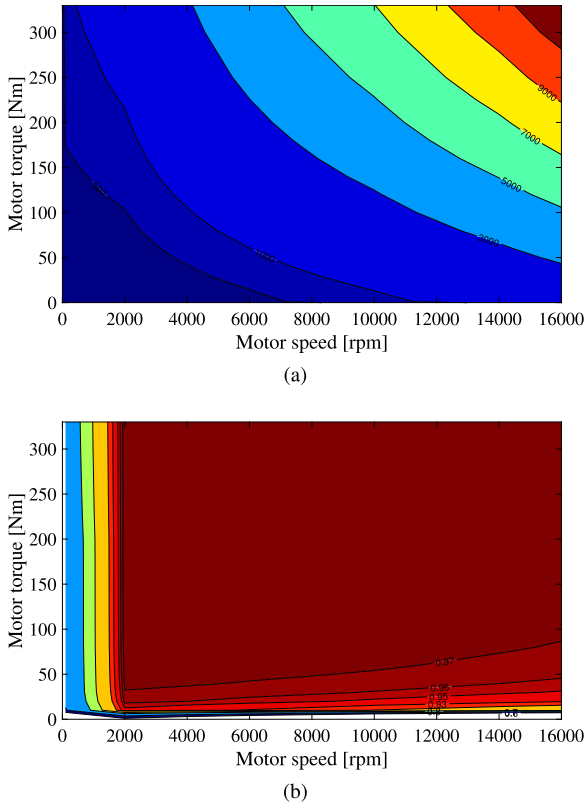

Fig. 6. Transmission data measured at 70° oil temperature: (a) loss map and (b) efficiency map.

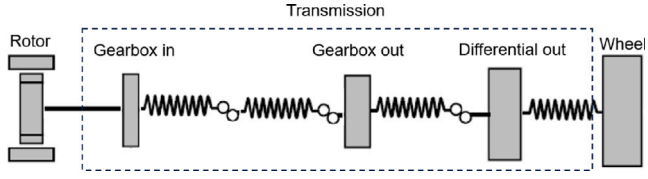

Fig. 7. Transmission torsional connections.

3. Torque modulation technique

3.1. Operating principle

In the case of a low torque demand, the torque modulation technique can be activated to potentially enhance the overall efficiency of the powertrain. As depicted in Fig. 8, the desired torque demand is modulated into a pattern of alternating between zero and a higher amplitude at a specific modulation frequency, denoted as f_{mod}. Within each modulation period, T_{mod}, the on-state torque, T_{on} lasts for a certain duration, t_{on}, followed by the off-state when the inverter is switched off. To maintain the same averaged output torque, the relation between the raw torque demand and the modulated torque can be described as

$$T_{\text{dem}} = \frac{t_{\text{on}}}{T_{\text{mod}}} \cdot T_{\text{on}} = D \cdot T_{\text{on}} \tag{2}$$

where T_{dem} is the raw powertrain torque demand in reference to motor and D is the modulation duty cycle which is defined as $\frac{t_{\text{on}}}{T_{\text{mod}}}$.

From an overall powertrain perspective, each component might exhibit distinct loss characteristics in response to such an operation, which is described in the following.

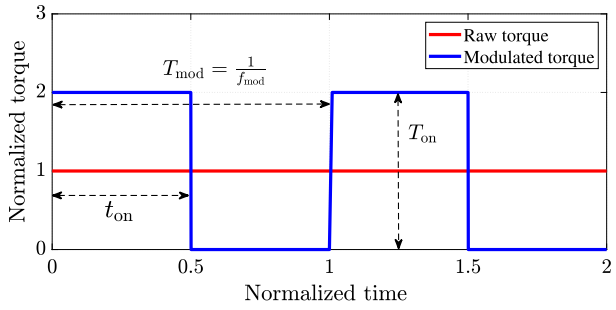

Fig. 8. Illustration of torque modulation technique with a duty cycle, D, of 0.5.

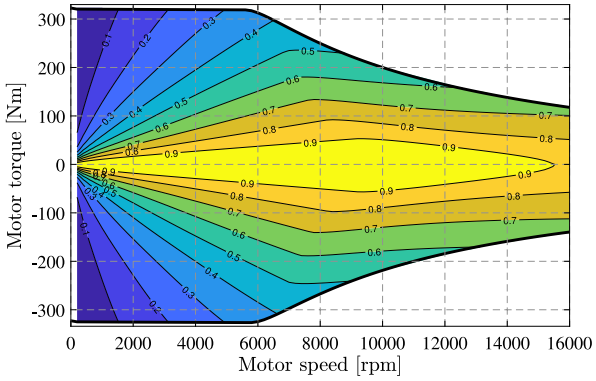

Fig. 9. Relative proportion of iron losses to the sum of iron and copper losses.

3.1.1. IPMSM

The torque generated by an IPMSM consists of magnetic torque and reluctance torque which are linear and quadratic functions of the dq stator current according to

$$T_{\text{m}} = \frac{3n_p}{2}\left[\psi_{\text{PM}} i_{\text{q}} - \left(L_{\text{d}} - L_{\text{q}}\right) i_{\text{d}} i_{\text{q}}\right] \tag{3}$$

where T_{m} is the mechanical torque of motor, n_p is the number of pole pairs, ψ_{PM} is the permanent magnet flux linkage, i_{d} is the d-axis current, i_{q} is the q-axis current, L_{d} is the d-axis inductance, and the L_{q} is the q-axis inductance.

The resistive copper losses in the motor windings quadratically increase with the stator currents as

$$P_{\text{cu}} = \frac{3}{2} {I_{\text{o}}}^2 R_{\text{s}} \tag{4}$$

where P_{cu} are the motor copper losses, I_{o} is the peak phase current, and R_{s} is the winding resistance. This suggests that the torque modulation will increase the motor copper losses by a factor of $(\frac{1}{D})^2 \cdot D = \frac{1}{D}$ compared to the no-modulation case for the linear term in (3). In contrast, for the quadratic term of (3), the copper loss remains unchanged with torque modulation $((\frac{1}{\sqrt{D}})^2 \cdot D = 1)$. As a result, it can be concluded that the total copper losses of the motor are increased with torque modulation. However, the iron loss can be reduced when switching off the inverter as shown in Fig. 5. In the low torque region where the iron losses are more dominant (shown in Fig. 9), the overall loss of the IPMSM can be reduced with the torque modulation technique.

3.1.2. Inverter

The loss of an IGBT-based three-phase inverter consists of conduction loss and switching loss as

$$P_{\text{inv}} = \overbrace{A {I_{\text{o}}}^2 + B I_{\text{o}}}^{\text{Conduction loss}} + \overbrace{C I_{\text{o}}}^{\text{Switching loss}} \tag{5}$$

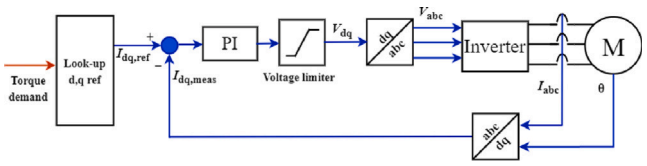

Fig. 10. Closed-loop current control with PI controller in dq-coordinates.

where P_{inv} is the inverter loss and A, B, C are lumped parameters including the loss parameters of the IGBTs and their antiparallel diodes. The losses in the inverter consist of a quadratic term and two linear terms relative to the current. Similar to the motor copper loss, the quadratic loss is increased while the linear terms such as the conduction loss due to voltage drop and switching loss can be reduced by the torque modulation technique.

3.1.3. Battery

For the first-order RC equivalent circuit, the battery ohmic loss can be estimated numerically when simplified as a pure resistive model as

$$P_b = 0.8 \cdot I_{dc}^2 \cdot (R_0 + R_1) \tag{6}$$

where I_{dc} is the DC current. Such resistive loss shares the same principle of motor copper loss, thus the battery loss is increased with the torque modulation technique. It should be noted that this simplification of the first-order RC battery model is only used for deriving the optimal modulation strategy in Section 4. As described in [32], a pure resistive model overestimates the battery losses by up to 20% compared to the first-order RC model used in powertrain system simulation. Hence a correction factor of 0.8 is used.

3.1.4. Transmission

As depicted in Fig. 6, the transmission achieves higher efficiency at higher torque demands which means the transmission losses can be reduced with the torque modulation technique.

3.2. Modulation frequency

The torque modulation frequency, f_{mod}, is constrained within specific upper and lower limits. On one hand, this frequency must not surpass the motor torque response time to ensure enough time for the motor to reach the desired T_{on} within the on-state duration, t_{on}. On the other hand, an excessively low modulation frequency should be avoided, as it may lead to discernible pulsating torque output which could potentially compromise driver comfort.

3.2.1. Upper limit

The motor torque response time is closely correlated to the corresponding current control. In this study, the commonly used proportional–integral (PI)-based current control loop (as shown in Fig. 10) and the deadbeat controller are investigated. The inverter switching frequency (f_{sw}) and sampling frequency (f_s) of 10 kHz are used, with the corresponding current control bandwidth of 1000 rad/s. Hence, the time constant τ for the torque response is 0.001 s [33]. The PI current controller is formed as a first-order system, referred to as H-infinity loop-shaping which shapes the open-loop frequency response of a system to optimize the system to handle disturbances and uncertainties effectively [34]. Thus, for PI-based current control, the torque response time (from 0% to 98.2% of the desired value) can be calculated as

$$t_{resp,PI} = 4\tau = 0.004 \text{ s} \tag{7}$$

The deadbeat controller serves as a promising alternative to be applied along with the torque modulation technique, since it calculates control actions at each sampling instant to reach the desired setpoint in minimal steps. Therefore, it pushes the torque response time of the discrete-time system to the limit set by the inverter switching frequency [33,35], achieving a much faster torque response time as

$$t_{resp,DB} = \frac{1}{f_{sw}} = 0.001 \text{ s} \tag{8}$$

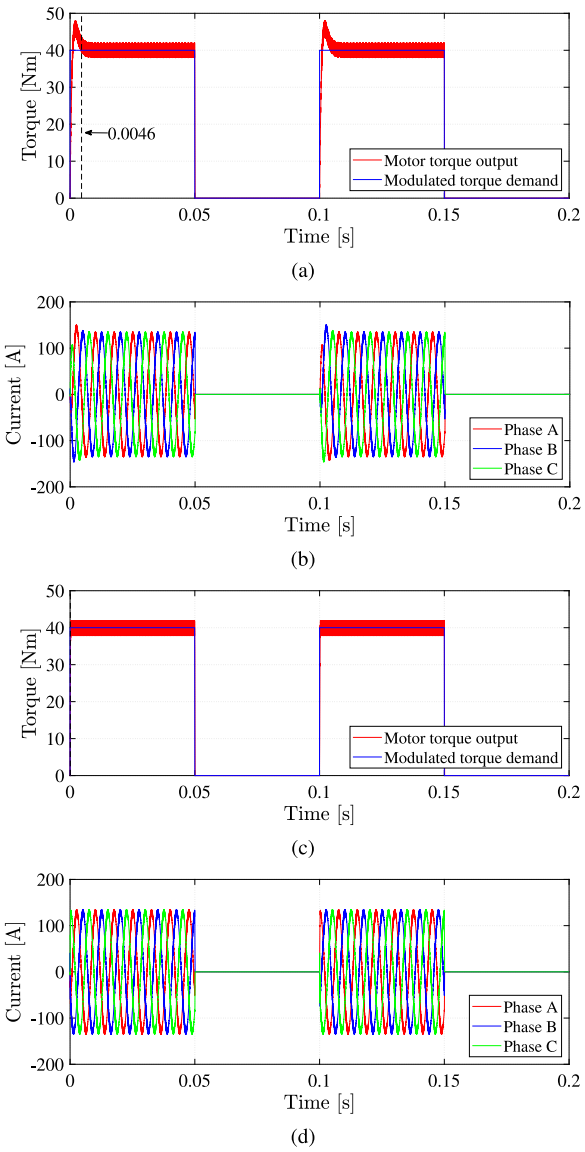

Fig. 11. Torque and three-phase current response of an example case where T_{dem} = 10 Nm, D = 0.5 and f_{mod} = 10 Hz: (a) Motor torque response with PI controller, (b) phase currents with PI controller, (c) motor torque response with deadbeat controller and (d) phase currents with deadbeat controller.

The PI and deadbeat current controller have been implemented in the model discussed in Section 2.3. The torque response time with the two current controllers is verified as shown in Fig. 11. Therefore, the theoretical maximum torque modulation frequencies for ensuring the motor has sufficient time to reach T_{on} within one modulation period T_{mod} for the PI controller and deadbeat controller are 250 Hz and 1000 Hz, respectively. However, since the on-state duration t_{on} can be significantly shorter than the duration of one modulation period T_{mod} in the case of a low modulation duty cycle, and the desired T_{on} needs to last for an adequate duration to effectively utilize the torque modulation strategy, it is advisable to keep the torque response time within 10% of one modulation period. Therefore, an appropriate upper

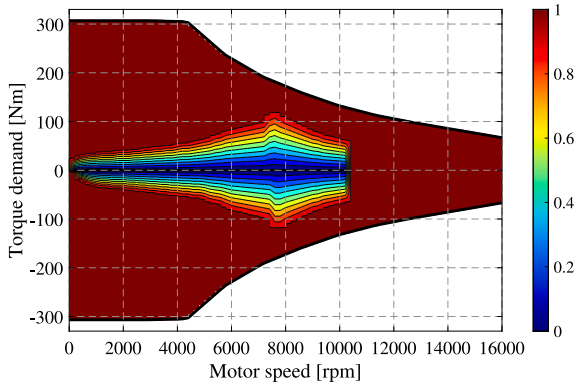

Fig. 12. Modulation duty cycle of single motor powertrain with DMD strategy.

limit for the modulation frequency can be determined as 25 Hz for the PI controller and 100 Hz for the deadbeat controller.

3.2.2. Lower limit

A low torque modulation frequency can lead to a perceived driver discomfort which is affected by the specific selection of the torque amplitude, T_{on}, as well as the modulation frequency, f_{mod}. This aspect is discussed in Section 5 in combination with a driver comfort evaluation and the torque modulation strategy.

4. Optimal modulation strategy

In this section, different considerations and the derivation of the optimal modulation strategies based on analytical powertrain and battery losses calculation for both single and dual motor powertrains are presented.

4.1. Single motor powertrain

In the DMD strategy proposed, the modulated torque amplitude, T_{on}, is defined by the highest-efficiency torque at each motor speed with a scaling factor due to the consideration of vibrations [16]. With such a strategy, the resulting modulation duty cycle across the powertrain operating region is shown in Fig. 12. However, this strategy might result in excessive battery losses. Therefore, the optimal modulation strategy should take into account the losses of the complete powertrain, including the battery, inverter, motor, and transmission. The overall powertrain loss (P_{pt}) during one torque modulation period consists of the losses occurring during both on- and off-states as

$$P_{pt} = \frac{\int_0^{DT_{mod}} \left(P_{on}\left(\omega, \frac{T_{dem}}{D}\right) + P_b \right) dt + \int_{DT_{mod}}^{T_{mod}} P_{no\text{-}load}(\omega) dt}{T_{mod}} \tag{9}$$

where ω is the motor angular velocity, P_{on} and $P_{no\text{-}load}$ are the EDU loss (combined loss of the inverter, motor and transmission) during the on- and off-state, respectively.

The battery losses can be further expressed as

$$\begin{aligned} P_b &= 0.8 \left(\frac{P_{dc}}{V_{dc}} \right)^2 (R_0 + R_1) \\ &= 0.8 \left[\frac{\frac{2\pi}{60}\omega \frac{T_{dem}}{D} + P_{on}\left(\omega, \frac{T_{dem}}{D}\right)}{V_{dc}} \right]^2 (R_0 + R_1) \end{aligned} \tag{10}$$

where P_{dc} is the battery terminal power and V_{dc} is the battery terminal voltage. It is worth noting that the nominal values of V_{dc}, R_0 and R_1 are used in the calculation with their dependency on the battery loading and SoC neglected for simplification. By combining (9) and (10), the overall powertrain losses of the single motor powertrain with torque modulation technique can be simplified to

$$\begin{aligned} P_{pt} &= D P_{on}\left(\omega, \frac{T_{dem}}{D}\right) \\ &+ 0.8D \left[\frac{\frac{2\pi}{60}\omega \frac{T_{dem}}{D} + P_{on}\left(\omega, \frac{T_{dem}}{D}\right)}{V_{dc}} \right]^2 (R_0 + R_1) \\ &+ (1 - D) P_{no\text{-}load}(\omega) \end{aligned} \tag{11}$$

Finally, for each powertrain operating point, the optimization problem that minimizes the overall powertrain loss with regard to the optimal torque modulation duty cycle can be generalized as follows

$$\begin{aligned} &\min\ P_{pt}(D) \\ &\text{s.t.} \\ &0 \le D \le 1 \\ &0 \le \omega \le 10200 \\ &T_{min}(\omega) \le \frac{T_{dem}}{D} \le T_{max}(\omega) \end{aligned} \tag{12}$$

The enumeration algorithm is chosen for this optimization task due to its systematic and exhaustive approach to finding the global optimal solution. While the exhaustive nature of the enumeration algorithm can lead to high computational costs for larger and more complex problems, it is well-suited for this specific optimization task given the simplicity of the objective function (11) in a single motor powertrain. Additionally, the computational burden is not prohibitive, making the enumeration algorithm an effective and feasible choice for searching all possible solutions.

For mapping the optimal modulation duty cycle in the whole operating range, the operating conditions are discretized into a finite combination of operating points. Specifically, the motor speed ω is discretized into a set of values ranging from 0 to 16000 rpm with increments of 100 rpm, resulting in the set $\{0, 100, 200, \ldots, 16000\}$ rpm. The torque demand T_{dem} is discretized into a set of values ranging from −310 Nm to 310 Nm with increments of 10 Nm, resulting in the set $\{-310, -300, -290, \ldots, 310\}$ Nm. These discretizations form a finite combination of operating points in a matrix of motor speed and torque demand. For each combination of discretized ω and T_{dem}, the algorithm evaluates P_{pt} over the discretized duty cycle D set from 0 to 1, discretized into suitable steps with increments of 0.01. Each potential solution is checked to ensure it satisfies all the constraints in (12). The objective function P_{pt} is evaluated for each feasible D value at every operating point (ω, T_{dem}). For each operating point, the D value that yields the minimum P_{pt} is selected as the optimal duty cycle D_{opt}.

After the optimization process for all the operating points, the optimal modulation duty cycle (D_{opt}) for each operating point is derived, as illustrated in Fig. 13. It is worth noting that the effective area of the torque modulation technique is significantly reduced compared to the modulation strategy proposed in the DMD, as the optimization of the modulation duty cycle considers the battery losses. This reduction is attributed to the fact that an excessive on-state torque, T_{on}, results in high battery pulsating loss. Consequently, the corresponding optimal T_{on} is no longer directly linked to optimal efficiency torque.

In addition, Fig. 14 illustrates the relative percentage of overall powertrain losses reduction achieved through torque modulation with an optimal modulation duty cycle, compared to regular operation without the torque modulation technique across various operating points within the effective area. It is evident that higher energy-savings potential with the torque modulation technique can be achieved at operating points with lower torque demand.

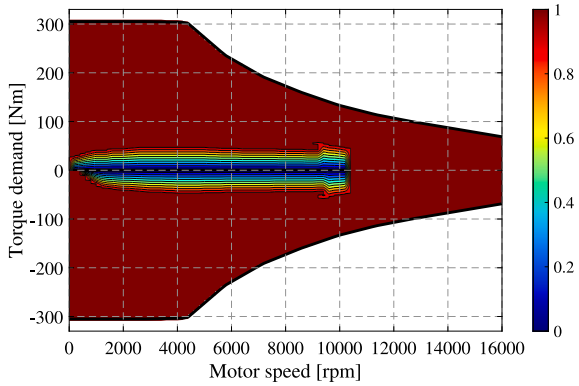

Fig. 13. Optimal modulation duty cycle of single motor powertrain.

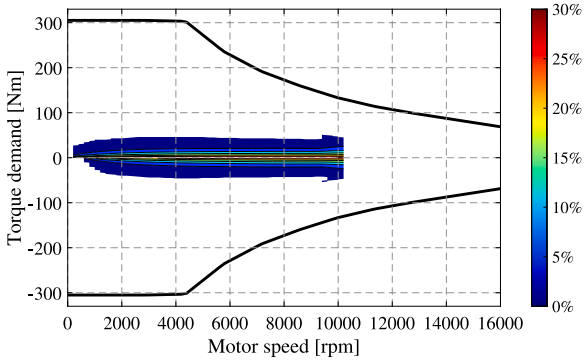

Fig. 14. Overall powertrain losses reduction percentage through torque modulation with an optimal modulation duty cycle.

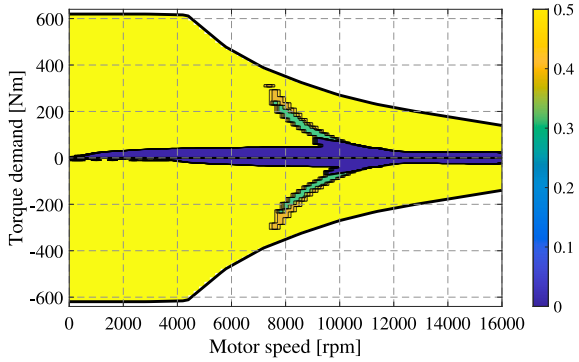

Fig. 15. Optimal torque distribution ratio for dual motor powertrain without torque modulation.

4.2. Dual motor powertrain

As an additional degree of freedom to optimize the powertrain efficiency, the dual motor powertrain offers a torque distribution capability by sharing the powertrain torque demand, T_{dem}, between the two motors. The optimal torque distribution ratio between the front and rear EDU is derived based on the numerical method detailed in [21] and shown in Fig. 15 without torque modulation.

Nevertheless, as demonstrated in the single motor powertrain, the lower the torque demand on the motor, the greater the potential for energy savings. It is noted that the dual motor powertrain can potentially utilize more of the energy-saving advantages compared to single motor powertrains since each EDU can individually operate at lower torque level. In principle, the implementation of the torque modulation technique in a dual motor powertrain should ensure complementary on-

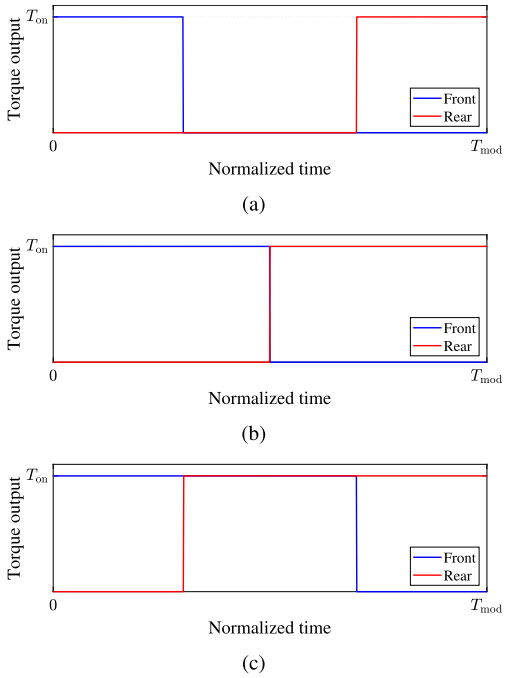

Fig. 16. Possible scenarios of torque modulation in a dual motor powertrain: (a) Scenario I: $D_{\text{f}} + D_{\text{r}} < 1$, (b) scenario II: $D_{\text{f}} + D_{\text{r}} = 1$ and (c) scenario III: $D_{\text{f}} + D_{\text{r}} > 1$.

and off-states between the two motors. That is, when one motor is in the on-state, the other should be in the off-state to prevent superimposed high powertrain torque outputs and intermittent battery currents, I_{dc}, and, thereby, avoiding increased battery losses and deteriorated driver comfort. This requires complementary Pulse Width Modulation (PWM) waveforms used for the front and rear motor. Depending on the modulation duty cycle of the front and rear motor (as denoted as D_{f} and D_{r}, respectively), three different scenarios can occur as illustrated in Fig. 16. In scenario I, where the sum of D_{f} and D_{r} is smaller than one, the front and rear motor have complementary on-state duration with a torque blanking time from between the respective on-states. Scenario II represents a specific scenario where the sum of the front and rear modulation duty cycles is exactly one, meaning that there is no torque blanking time from the powertrain. In addition, if both D_{f} and D_{r} are equal to 0.5, the front and rear motor have perfectly complementary modulation so that there is no torque fluctuation from the powertrain. While in scenario III, where the sum of D_{f} and D_{r}, is bigger than one, an overlapped modulation time occurs and both front and rear motors are simultaneously operating at on-state, resulting in a high torque output from the powertrain. This also leads to superimposed battery currents, hence amplified battery losses.

The overall powertrain losses of a dual motor powertrain with the torque modulation technique consist of the losses occurring during on- and off-states for both front and rear EDUs as

$$\begin{aligned} P_{\text{pt}} = \frac{1}{T_{\text{mod}}} \Bigg[& \int_0^{D_{\text{f}} T_{\text{mod}}} \left(P_{\text{on}} \left(\omega, T_{\text{f}} \right) \right) dt \\ & + \int_{D_{\text{f}} T_{\text{mod}}}^{T_{\text{mod}}} \left(P_{\text{no-load}} \left(\omega \right) \right) dt + \int_0^{D_{\text{r}} T_{\text{mod}}} \left(P_{\text{on}} \left(\omega, T_{\text{r}} \right) \right) dt \\ & + \int_{D_{\text{r}} T_{\text{mod}}}^{T_{\text{mod}}} \left(P_{\text{no-load}} \left(\omega \right) \right) dt \Bigg] + P_{\text{b}} \\ = {} & D_{\text{f}} T_{\text{mod}} P_{\text{on}} \left(\omega, T_{\text{f}} \right) + \left(2 - D_{\text{f}} - D_{\text{r}} \right) P_{\text{no-load}} \left(\omega \right) \\ & + D_{\text{r}} T_{\text{mod}} P_{\text{on}} \left(\omega, T_{\text{r}} \right) + P_{\text{b}} \end{aligned} \tag{13}$$

where T_f and T_r are the on-torque of front and rear EDU, respectively. Based on the three scenarios, the battery losses can be further expressed as

$$
\begin{aligned}
&\text{if } D_f + D_r \le 1: \\
&P_b = 0.8\left[D_f\left(\frac{\frac{2\pi}{60}\omega T_f + P_{on}(\omega, T_f)}{V_{dc}}\right)^2\right. \\
&\quad \left. + D_r\left(\frac{\frac{2\pi}{60}\omega T_r + P_{on}(\omega, T_r)}{V_{dc}}\right)^2\right](R_0 + R_1), \\
&\text{if } D_f + D_r > 1: \\
&P_b = 0.8\left[(1 - D_r)\left(\frac{\frac{2\pi}{60}\omega T_f + P_{on}(\omega, T_f)}{V_{dc}}\right)^2\right. \\
&\quad + (1 - D_f)\left(\frac{\frac{2\pi}{60}\omega T_r + P_{on}(\omega, T_r)}{V_{dc}}\right)^2 \\
&\quad \left. + \left(\frac{\frac{2\pi}{60}\omega(T_f + T_r) + P_{on}(\omega, T_f) + P_{on}(\omega, T_r)}{V_{dc}}\right)^2 \right. \\
&\quad \left. (D_f + D_r - 1)\right](R_0 + R_1)
\end{aligned}
\tag{14}
$$

Thus, the optimization problem can be formulated as

$$
\begin{aligned}
&\min P_{pt}(D_f, D_r, T_f, T_r) \\
&\text{s.t.} \\
&0 \le D_f \le 1 \\
&0 \le D_r \le 1 \\
&0 \le \omega \le 10200 \\
&T_{min}(\omega) \le T_f \le T_{max}(\omega) \\
&T_{min}(\omega) \le T_r \le T_{max}(\omega) \\
&D_f T_f + D_r T_r = T_{dem}
\end{aligned}
\tag{15}
$$

Unlike the optimization problem for the single motor powertrain, the cost function for the dual motor powertrain (13) involves more variables with conditional expressions associated with battery loss (14). The enumeration algorithm can lead to exponentially increasing computational effort due to the large number of variables and conditional constraints. Therefore, the Particle Swarm Optimization (PSO) algorithm is used for identifying the optimal D_f, D_r, T_f and T_r for each powertrain operating point as it is particularly suitable for such complex non-linear optimization problem with conditional expressions due to its ability to efficiently explore large and complex search spaces [36]. The initial guess is set as $D_f = D_r = 0.5$ and $T_f = T_r = T_{dem}$ for each operating point. Throughout the optimization process, constraints in (15) are enforced to ensure feasible solutions.

After the optimization process for all the operating points, it is found that the optimal solution yields $D_f = D_r$ and $T_f = T_r$ for all the operating points due to the identity of the EDUs. Hence, for dual motor powertrain, the optimal modulation strategy can be expressed as $D_f = D_r = D_{opt}$ and $T_f = T_r = \frac{T_{dem}}{2D_{opt}}$. Fig. 17 shows the optimal modulation duty cycle (D_{opt}) for both front and rear motor. Compared to a single motor powertrain, the effective area of the torque distribution technique is expanded. The powertrain operates predominantly as in scenario I in the low torque demand area. In contrast, in areas characterized by low speed but medium torque demand, scenario III becomes the preferred mode of operation with reduced overall powertrain losses despite an increase in the battery losses. Notably, as the operating speed increases, the optimal modulation duty cycle is limited to a maximum of 0.5 (as in scenario II) since the excessive battery losses caused by the superimposed battery current, I_{DC}, becomes significant within the powertrain.

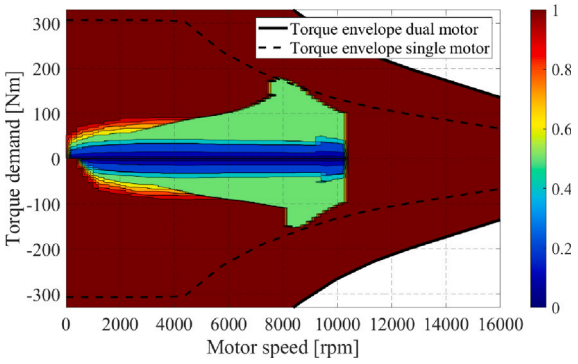

Fig. 17. Optimal modulation duty cycle of dual motor powertrain with $T_f = T_r = \frac{T_{dem}}{2D}$.

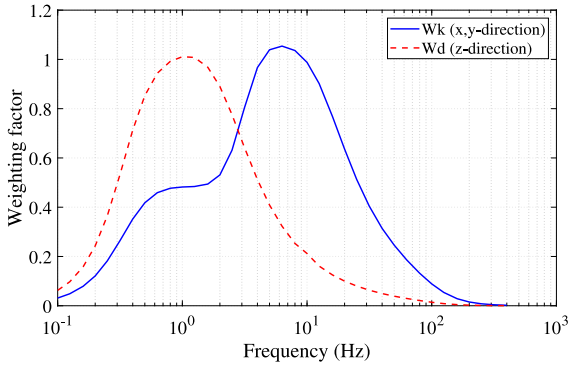

Fig. 18. ISO2631 frequency weighting curves.

Table 2
Approximate indications of likely reactions to various VTV values.

Acceleration (m/s^2)	Comfort level
Less than 0.315	Not uncomfortable
0.315–0.63	A little uncomfortable
0.5–1	Fairly uncomfortable
0.8–1.6	Uncomfortable
1.25–2.5	Very uncomfortable
Greater than 2	Extremely uncomfortable

5. Driver comfort evaluation

As mentioned in Section 3.2.2, the driver comfort level is determined by the on-state torque amplitude together with the modulation frequency. In this section, the resultant driver discomfort level is examined for the torque modulation strategies derived in the previous section for both single and dual motor powertrains.

The discomfort level can be quantified as Vibration Total Value (VTV) according to ISO2631-1, "Mechanical vibration and shock - Evaluation of human exposure to whole-body vibration - Part 1: General requirements", which indicates the potential impact of vibrations on human discomfort by considering factors such as the magnitude of the vibration, its frequency, the direction of vibration, as well as the duration of exposure. The ISO2631-1 also lists the reference VTV values used to assess the discomfort level as given in Table 2.

The frequency-weighted Root-Mean-Square (RMS) acceleration, a_w, can be derived as

$$
a_w = \sqrt{\sum_i (w_i a_i)^2} \tag{16}
$$

where a_i is the RMS acceleration for the corresponding frequency and w_i is the weighting factor for each frequency, as shown in Fig. 18.

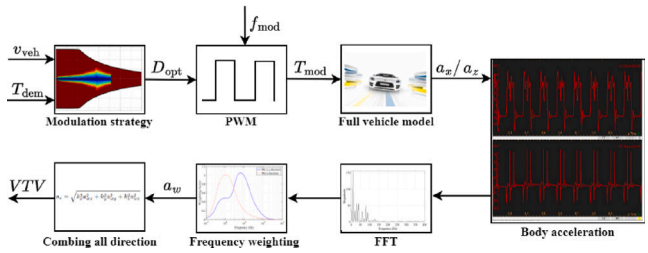

Fig. 19. Calculation of VTV value.

The vibration total value, a_v, combining the vibration in all directions, is then assessed at the vehicle center of gravity as

$$a_v = \sqrt{k_x^2 a_{wx}^2 + k_y^2 a_{wy}^2 + k_z^2 a_{wz}^2} \tag{17}$$

where a_{wx}, a_{wy}, a_{wz} are the frequency-weighted RMS accelerations with respect to the orthogonal axes x, y and z, respectively; k_x, k_y, k_z are the weighing factors.

A full vehicle model of the considered vehicle is utilized in IPG CarMaker to calculate the body acceleration caused by the pulsating torque output from the powertrain, including effects such as suspension damping and tire deformation. Though in real-world applications external disturbances such as road roughness can be transmitted through the tire, suspension and vehicle and cause discomfort independently or interact in complex ways with the internal pulsating torque, they are excluded in the analysis in this section to ensure a controlled relative comparison as the primary focus is to evaluate the impact of torque modulation technique on driver comfort.

To evaluate the discomfort level associated with the torque modulation technique, the VTV is calculated and mapped across the entire powertrain operating range within the effective torque modulation area, following the procedure illustrated in Fig. 19. For each operating point, the vehicle is initialized at the corresponding speed in the simulation setup. The torque demand is then modulated based on the optimal modulation duty cycle at a certain modulation frequency for that operating point, and subsequently sent to the EDU. The resulting body acceleration at the vehicle's center of gravity is recorded over 10 modulation periods. As lateral movement is not considered in this study, only the longitudinal (x) and vertical (z) accelerations are logged. A Fast Fourier Transformation (FFT) is then applied to the recorded accelerations, and frequency weighting factors are used to calculate the frequency-weighted RMS accelerations in the x and z directions, as described in (16). Finally, the VTV is derived by combining the frequency-weighted RMS accelerations in the x and z directions according to (17).

The VTV values of a single motor powertrain with DMD strategy and the proposed optimal modulation strategy at different torque modulation frequencies are presented in Fig. 20 and Fig. 21, respectively. It is observed that at lower modulation frequencies, such as 10 Hz and 15 Hz, the VTV values can exceed 0.315, leading to perceptible discomfort caused by the torque modulation at certain operating points. However, it is noteworthy that an increase in modulation frequency tends to reduce the overall VTV values. Specifically, when the modulation frequency is augmented to 20 Hz, the level of driver discomfort becomes imperceptible throughout the entire operating range. This indicates that for a single motor powertrain implementing the DMD strategy, the lower limit of modulation frequency is about 20 Hz given constant modulation frequency throughout the entire operating region. In contrast, employing the proposed optimal modulation strategy significantly reduces VTV values. Consequently, even at a modulation frequency of 10 Hz, the perceived discomfort is effectively eliminated.

Similarly, the VTV values of the dual motor powertrain with optimal modulation strategy are shown in Fig. 22. It can be seen that the VTV values for the dual motor powertrain are consistently lower compared

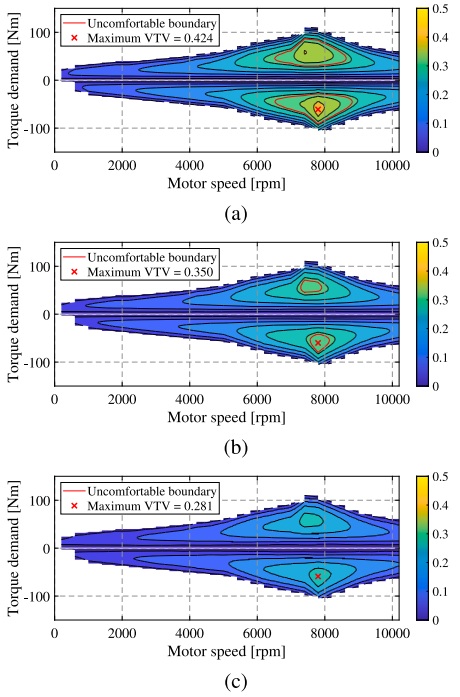

Fig. 20. VTV values of single motor powertrain with DMD strategy at different torque modulation frequencies: (a) 10 Hz, (b) 15 Hz and (c) 20 Hz.

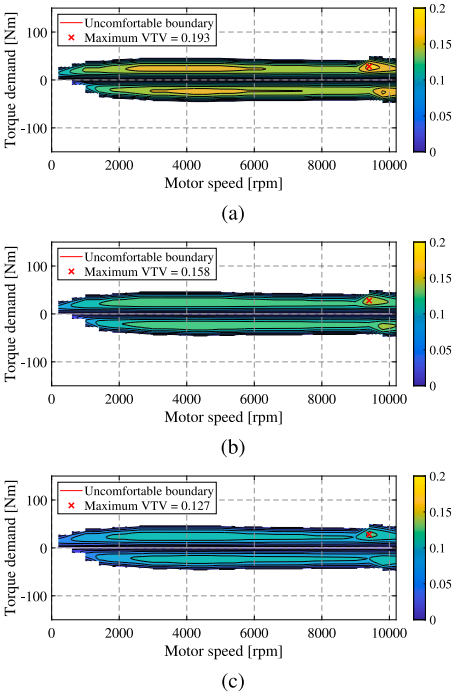

Fig. 21. VTV values of single motor powertrain with optimal modulation strategy at different torque modulation frequencies: (a) 10 Hz, (b) 15 Hz and (c) 20 Hz.

to the single motor configuration since both motors modulate at lower torque demands. Notably, even at peak VTV values, where the torque modulation strategy operates under scenario III (overlapped on-states of the front and rear motors), the VTV values remain below the threshold of perceived discomfort with a low modulation frequency of 10 Hz.

Table 3
Drive-cycle energy consumption of single motor powertrain.

Control strategy	WLTC		LS cycle		HS cycle	
	Energy cons. [kWh/100 km]	Difference	Energy cons. [kWh/100 km]	Difference	Energy cons. [kWh/100 km]	Difference
No modulation	19.68	–	13.52	–	21.71	–
DMD modulation strategy	19.55	−0.66%	13.37	−1.11%	21.74	+0.14%
Optimal modulation strategy	19.47	−1.05%	13.36	−1.18%	21.57	−0.78%

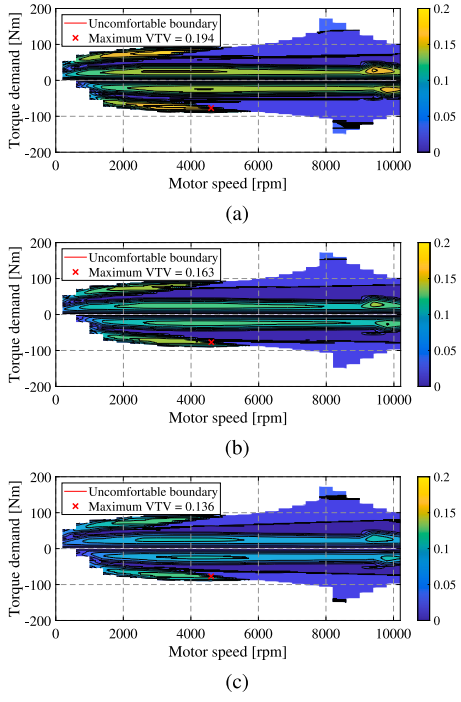

Fig. 22. VTV values of dual motor powertrain with optimal modulation strategy at different torque modulation frequencies: (a) 10 Hz, (b) 15 Hz and (c) 20 Hz.

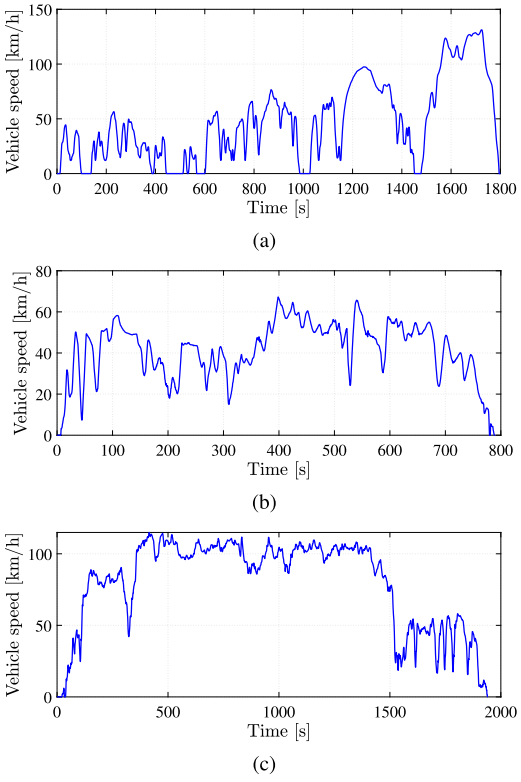

Fig. 23. Drive cycle vehicle speed profiles: (a) WLTC, (b) LS and (c) HS.

Moreover, in the area where the modulation strategy operates under scenario II (perfectly complementary on- and off-state of the front and rear motors), the modulation-induced vibration is almost negligible.

6. Impact on drive-cycle energy efficiency

In this section, the energy efficiency improvements are studied through powertrain system simulation. Specifically, three drive cycles are analyzed (shown in Fig. 23): the WLTC as a standard test cycle, along with two real-world drive cycles representing urban Low-Speed (LS) driving and highway High-Speed (HS) driving scenarios. The data collection of the real-world drive cycles are detailed in [37]. In addition, the unmodulated drive-cycle operating points together with effective area of different modulation strategies are illustrated in Fig. 24

6.1. Single motor powertrain

In addition to the proposed optimal modulation strategy, two other cases are considered: regular operation without torque modulation technique and DMD modulation strategy. Besides, the modulation frequency of 20 Hz is employed with a PI current controller. The energy consumptions of single motor powertrain over the investigated drive cycles are summarized in Table 3. In addition, the detailed powertrain losses are broken down into each component and presented in Fig. 25.

The DMD strategy effectively reduces energy consumption compared to regular operation without torque modulation in both the WLTC and LS drive cycles. Additionally, the reduction in energy consumption for the WLTC drive cycle achieved by the DMD strategy aligns

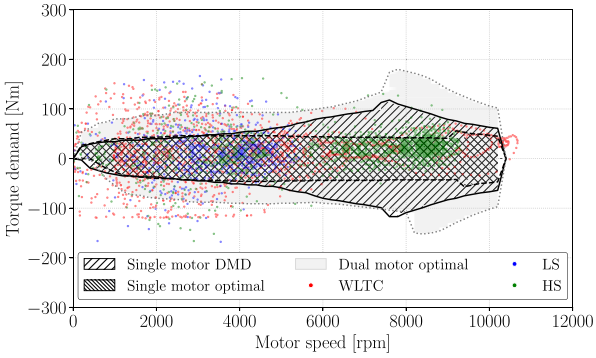

Fig. 24. Unmodulated operating points of the investigated drive cycle over the effective areas of the torque modulation strategies.

with the values reported in [16]. However, in the HS drive cycle, the DMD strategy results in higher energy consumption compared to regular operation without torque modulation. This increase is due to the DMD strategy not accounting for the potential excessive battery loss induced by pulsating currents. Consequently, although losses in the inverter, motor and transmission are reduced across all the drive cycles, there is a notable increase in battery losses, as shown in Fig. 25. In the HS drive cycle, which demands higher power with high speed, pulsating currents lead to significantly increased battery losses, ultimately raising the overall powertrain losses. In contrast, the optimal modulation

Table 4
Drive-cycle energy consumption of dual motor powertrain.

Control strategy	WLTC		LS cycle		HS cycle	
	Energy cons. [kWh/100 km]	Difference	Energy cons. [kWh/100 km]	Difference	Energy cons. [kWh/100 km]	Difference
No modulation	20.78	–	14.45	–	22.97	–
Optimal modulation strategy	20.32	−2.21%	14.04	−2.84%	22.54	−1.87%

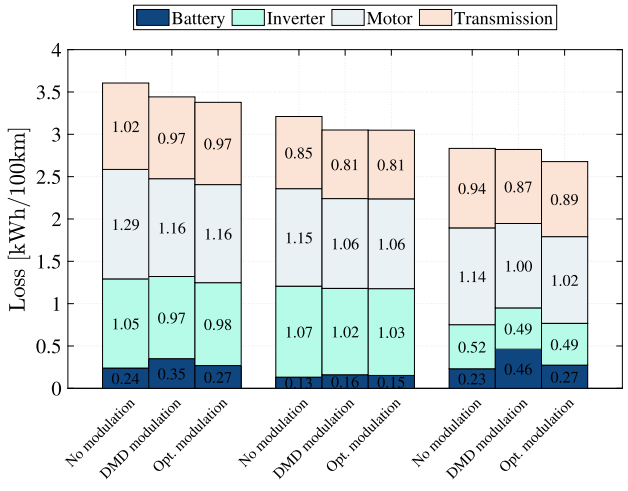

Fig. 25. Single motor powertrain drive-cycle losses breakdown.

strategy, which considers battery and transmission losses, results in slightly higher losses in the inverter, motor and transmission compared to the DMD strategy due to its less aggressive and more gradual torque modulation. However, it significantly reduces battery losses. This reduction in battery loss outweighs the marginally increased losses in other powertrain components, leading to a reduction in overall powertrain losses and maximizing overall powertrain efficiency. Moreover, as indicated in Fig. 24, the greatest discrepancy between the DMD strategy and the optimal modulation strategy occurs under high-speed operating conditions. In low-speed operating conditions, the difference between the two strategies is minimal. Therefore, for the HS drive cycle, the optimal modulation strategy demonstrates a higher energy-saving potential compared to the DMD strategy, while in the LS drive cycle, the energy-saving potentials between the two strategies are nearly identical.

6.2. Dual motor powertrain

For the dual motor powertrain operated without torque modulation or when the operating conditions outside the effective torque modulation range, the torque distribution functionality is utilized as detailed in Section 4.1. The energy consumptions of dual motor powertrain over the investigated drive-cycles are summarized in Table 4.

It is evident that the dual motor powertrain exhibits higher energy consumption compared to its single motor counterpart, primarily due to the increased no-load losses (motor iron loss and transmission drag loss) introduced by an additional EDU, as concluded in [21]. Nevertheless, the energy consumption reduction with torque modulation of the dual motor powertrain is significantly increased to 2.21%, 2.84% and 1.87% for the WLTC, LS and HS drive cycle, respectively. This implies that the application of the torque modulation technique can achieve higher energy-saving potentials in dual motor powertrains compared to single motor powertrains. This increased efficiency in the dual motor powertrain is attributable, firstly, to the broader effective modulation area, which encompasses more operating conditions. Consequently, the torque modulation technique can be utilized for 75.4%, 91.0% and 95.1% of the time during the WLTC, LS and HS drive cycle, respectively. In contrast, for a single motor powertrain with optimal modulation strategy, torque modulation is applicable for only 56.1%, 75.7% and 81.3% of the drive-cycle duration, as depicted in Fig. 24. Secondly, the effectiveness of the torque modulation technique is further amplified when the torque demand is lower. In a dual motor powertrain, the capability to distribute torque between two EDUs effectively halves the torque demand on each unit. This distribution results in a more efficient utilization of the torque modulation technique.

6.3. Effect of modulation frequency and current controller

As discussed in Section 3.2.1, the performance in following the ideal pulsating torque of the torque modulation strategy is affected by the selection of the current controller and torque modulation frequency. For the torque modulation technique implemented with a PI current controller, the transient period before the motor reaches the desired T_{on} leads to non-ideal transient energy loss in one modulation period. As the torque modulation frequency increases, the transient energy loss can accumulate drastically since the number of transient periods is proportional to the torque modulation frequency, eventually leading to noticeably deteriorated energy consumption as shown in Fig. 26. In the case of single motor powertrain, the WLTC drive-cycle energy consumption is increased by up to 0.23% when the torque modulation frequency rises from 10 Hz to 100 Hz. This impact is even more pronounced in a dual motor powertrain, where energy consumption increases by 0.67% over the same frequency range. This greater impact is due to the higher number of torque modulation events occurring in the dual motor powertrain, which uses two EDUs for torque modulation. As a result, the torque modulation frequency has around three times the impact on the increase of energy consumption for the dual motor powertrain (0.0015 kWh/100 km/Hz) compared to the single motor powertrain (0.0005 kWh/100 km/Hz) when using PI current controllers.

On the contrary, since the deadbeat current controller has a much faster motor torque response time, the transient period and the corresponding non-ideal transient energy loss can be minimized to negligible levels. Therefore, the drive-cycle energy consumption remains unaffected by the torque modulation frequency. Additionally, because the deadbeat current controller mitigates the non-ideal transient energy loss, it shows slightly lower WLTC drive-cycle energy consumption compared to the PI current controller, with reductions of 0.06% and 0.16% for single motor powertrain and dual motor powertrain at 20 Hz, respectively.

7. Impact on powertrain durability

In this section, the impact of torque modulation strategy on powertrain durability is assessed and demonstrated in the single motor powertrain using the optimal modulation strategy. Here, the WLTC drive cycle is utilized for load collective (the accumulation of varying loads experienced by the component over time for evaluating fatigue and durability) due to its comprehensive combination of low, medium, high, and extra high-speed driving conditions. With the torque modulation technique, the rotor shaft generates pulsating torque which propagates through the entire powertrain system, resulting in different torque harmonics due to the torsional effects of the transmission [38, 39]. Fig. 27 illustrates the rotor torque and differential ring gear torque for the 50 km/h constant speed driving scenario at different modulation frequencies. It indicates that higher torque modulation frequency can lead to reduced amplitude of torque variation in the powertrain, though with higher number of torque fluctuation cycles. The varying load can

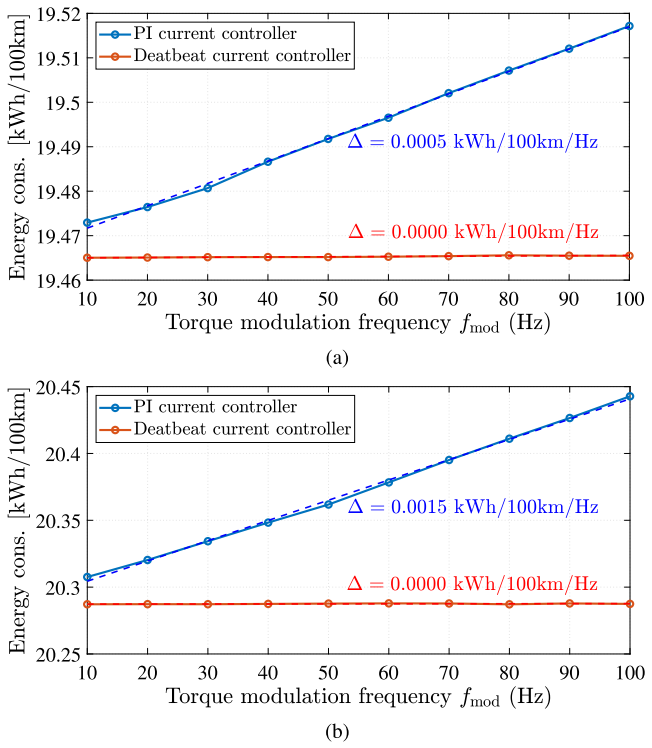

Fig. 26. WLTC drive-cycle energy consumption in relation to current controller and torque modulation frequency: (a) single motor powertrain and (b) dual motor powertrain.

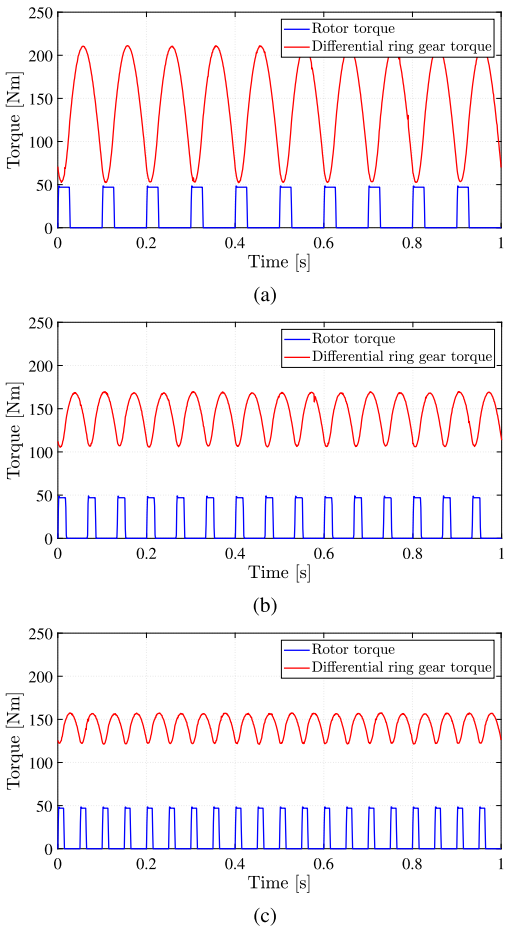

Fig. 27. Powertrain torques exemplified in 50 km/h constant speed driving scenario at different torque modulation frequencies: (a) 10 Hz, (b) 15 Hz and (c) 20 Hz.

contribute to different levels of fatigue damage in each part of the powertrain [40].

To conduct relative comparisons of durability between powertrains operating with and without the torque modulation technique, a simplified fatigue damage value - Duty Value (DV) is used as an indicator to describe the load's contribution to fatigue damage in powertrain components [41,42]. The DV is mainly used for relative comparisons of load collectives and is independent of component geometry and fatigue limit of the material. Specifically, two different types of DVs - Rotations At Level (RAL) and Torque Variation (TV) are assessed in this paper [43]. RAL describes the steady state load's influence on the fatigue life of gears and bearings amongst other components [44]. The DV for RAL is calculated as

$$DV_{\mathrm{RAL}} = \sum_i n_i \cdot T_i^{We} \tag{18}$$

where n_i is the number of rotations at torque level i, T_i is the torque level i in the load collective and We is the Wöhler exponent. The Wöhler exponent relates to the slope of the S-N curve, which is a graphical representation of the relationship between the cyclic stress (S) applied to a material and the number of cycles to failure (N). In this paper, a Wöhler exponent of 6 is used for steel components subject to torsional loading.

On the other hand, TV describes the varying load's influence on the fatigue life of casings amongst other components. The DV for TV is calculated as

$$DV_{\mathrm{TV}} = \sum_i s_i \cdot T_{Amp_i}^{We} \tag{19}$$

where T_{Amp_i} is the amplitude of the torque shift and s_i number of torque shift. Both T_{Amp_i} and s_i are obtained by rainflow counting method, which breaks down the load-time history into individual stress cycles, facilitating the assessment of fatigue damage [45].

In addition, the fatigue damage at rotor shaft as powertrain input torque and the fatigue damage at differential ring gear as the powertrain output torque are of particular interest since the two spots represent two extremes: where the pulsating torque is not filtered at all and where the pulsating torque is filtered through the transmission. Fig. 28 and Fig. 29 illustrate the number of rotations over different torque levels and the rainflow matrices at both rotor shaft and differential ring gear at different torque modulation frequencies. The resulting DV_{RAL} and DV_{TV} are listed in Table 5.

Fig. 28 reveals that at the rotor shaft, the torque modulation technique leads to concentrated rotations at zero and 40-50 Nm torque levels. These torque levels correspond to the T_{on} of the optimal modulation strategy. This concentration results in an increased DV_{RAL} at low torque levels within the effective area of the optimal torque modulation strategy. However, the spectrum of rotation numbers at high torque levels remains unaffected by the torque modulation. Since DV_{RAL} is primarily influenced by the torque levels (with a Wöhler exponent of 6), the corresponding excessive fatigue damage at low torque levels only has a minor impact on the overall DV_{RAL} across all torque levels, with a marginal increase of 1.53% compared to regular operation without torque modulation. As the rotor torque directly reflects the modulated pulsating torque without any torsional filtering, the torque modulation frequency does not substantially change the distribution of the number of rotations over the torque levels, and therefore shows no impact on DV_{RAL} at the rotor shaft. For the differential ring gear, the torque modulation technique has an almost negligible impact on DV_{RAL}. The increases are 0.20%, 0.08% and 0.04% for modulation frequencies of 10 Hz, 15 Hz and 20 Hz, respectively, compared to regular operation without torque modulation. This minimal impact is due to the torsional effects of the powertrain mechanism, which effectively filter the pulsating torque.

Table 5
Summary of DV.

Damage type	Assessed component	No modulation	10 Hz	Difference	15 Hz	Difference	20 Hz	Difference
DV_{RAL}	Rotor shaft	1.434×10^{16}	1.459×10^{16}	+1.53%	1.459×10^{16}	+1.53%	1.459×10^{16}	+1.53%
	Differential ring gear	2.446×10^{21}	2.451×10^{21}	+0.20%	2.448×10^{21}	+0.08%	2.447×10^{21}	+0.04%
DV_{TV}	Rotor shaft	6.807×10^{13}	7.172×10^{13}	+5.36%	7.293×10^{13}	+7.14%	7.427×10^{13}	+9.11%
	Differential ring gear	1.339×10^{20}	1.342×10^{20}	+0.22%	1.341×10^{20}	+0.15%	1.340×10^{21}	+0.07%

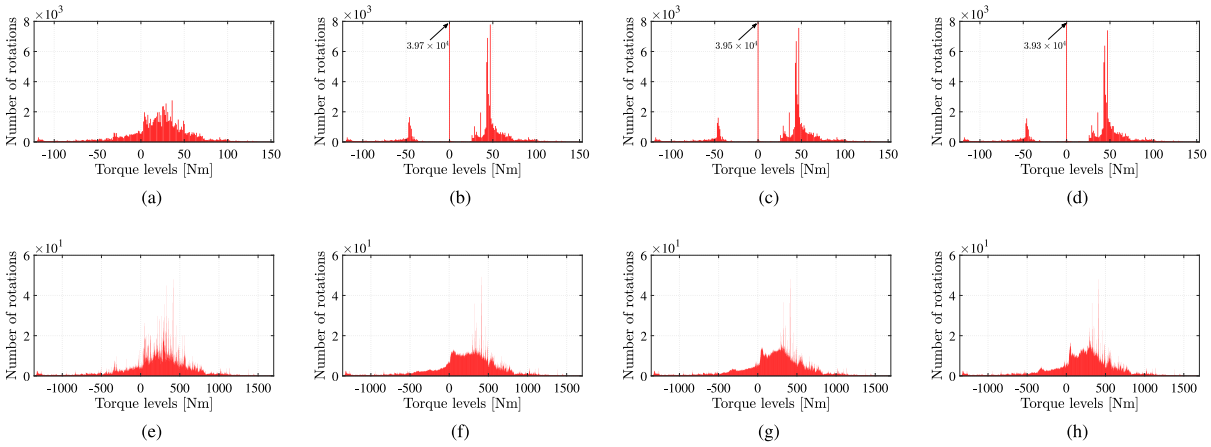

Fig. 28. Number of rotations at different torque levels: (a) rotor shaft without torque modulation, (b) rotor shaft with torque modulation at 10 Hz, (c) rotor shaft with torque modulation at 15 Hz, (d) rotor shaft with torque modulation at 20 Hz, (e) differential ring gear without torque modulation, (f) differential ring gear with torque modulation at 10 Hz, (g) differential ring gear with torque modulation at 15 Hz and (h) differential ring gear with torque modulation at 20 Hz.

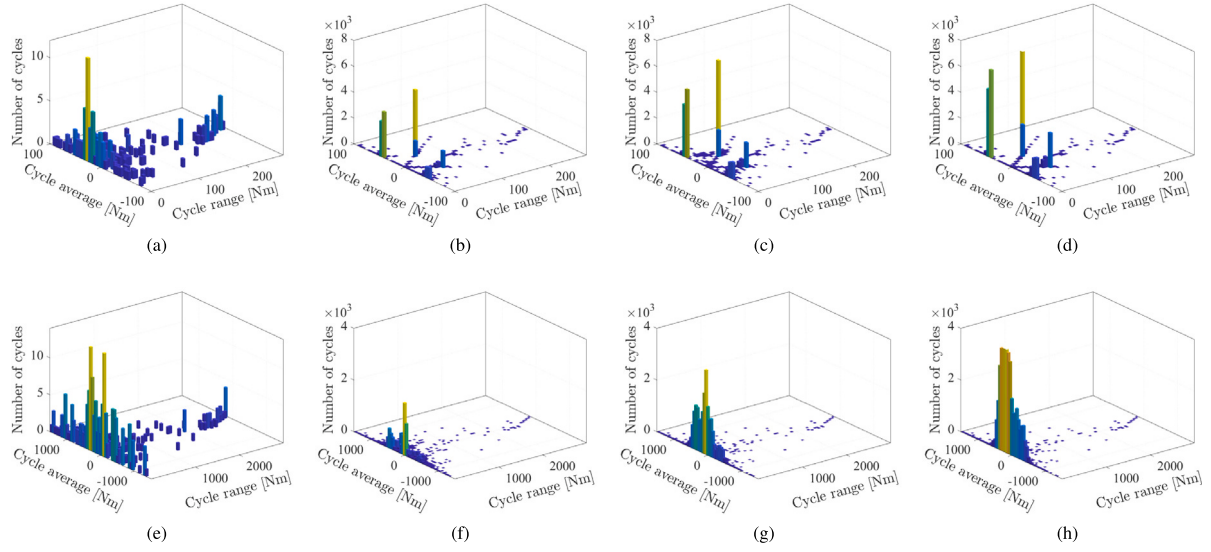

Fig. 29. Rainflow matrices: (a) rotor shaft without torque modulation, (b) rotor shaft with torque modulation at 10 Hz, (c) rotor shaft with torque modulation at 15 Hz, (d) rotor shaft with torque modulation at 20 Hz, (e) differential ring gear without torque modulation, (f) differential ring gear with torque modulation at 10 Hz, (g) differential ring gear with torque modulation at 15 Hz and (h) differential ring gear with torque modulation at 20 Hz.

As observed in Fig. 29, the torque modulation technique results in a significantly higher number of cycles for torque variation at the rotor shaft by alternating between zero and the optimal T_{on}. The number of cycles in the load cycle due to torque modulation is naturally proportional to the modulation frequency. Consequently, DV_{TV} is increased by 5.36%, 7.14% and 9.11% compared to regular operation without torque modulation for modulation frequencies of 10 Hz, 15 Hz, and 20 Hz, respectively. Similar to the fatigue damage resulting from RAL, the torque modulation technique results in only a marginal increase in DV_{TV} at the differential ring gear as the torque fluctuation is largely filtered by the torsional effects of the powertrain mechanism, with an increase of 0.22%, 0.15%, and 0.07% compared to regular operation without torque modulation when using the optimal torque modulation strategy at 10 Hz, 15 Hz, and 20 Hz, respectively. Though higher frequency reduces DV_{TV} at the differential ring gear, the changes are minimal.

In general, the torque modulation strategy primarily affects the rotor shaft by concentrating rotations at low torque levels and increasing the number of cycles for torque variation. Despite these increases, the overall impact on fatigue damage remains minimal because the torque modulation technique is only applicable in low torque operating conditions. The resulting fatigue damage is insignificant compared to the fatigue damage induced by regular operation at medium and high

torque levels, which are outside the effective area of the torque modulation technique. At the differential ring gear, the torsional effects of the powertrain mechanism effectively filter the pulsating torque, resulting in negligible changes in fatigue damage. This suggests that while torque modulation can influence the distribution of torque levels and cycles, the overall impact on powertrain durability is limited, particularly at the differential ring gear.

8. Conclusion

This paper proposed optimal modulation strategies for the torque modulation technique in BEV powertrains equipped with IPMs to enhance powertrain efficiency without compromising driver comfort and powertrain durability. Additionally, the application and potential of the torque modulation technique for both single and dual motor powertrains were investigated. The main findings are summarized as follows:

(i) The optimal modulation strategy achieves a 1.05% reduction in WLTC drive-cycle energy consumption for the single motor powertrain, while keeping driver discomfort within acceptable levels.

(ii) In dual motor powertrains, the energy-saving potential is more substantial, achieving a 2.21% reduction in WLTC drive-cycle energy consumption. The complementary operation of the two motors makes the impact of pulsating torque on driver discomfort almost negligible.

(iii) The torque modulation technique shows no significant negative impact on durability.

The findings particularly underscore the greater potential of dual motor powertrains in achieving further improvements in both efficiency and comfort. Additionally, the results offer insights into the integration of powertrain topology design with control optimization to maximize overall powertrain efficiency, providing a promising direction for future BEV powertrain developments.

CRediT authorship contribution statement

Y. Xu: Writing – original draft, Software, Methodology, Formal analysis, Conceptualization. **P. Ingelström:** Methodology, Conceptualization. **A. Kersten:** Writing – review & editing, Formal analysis. **A. Andersson:** Methodology, Data curation. **S. Klacar:** Writing – review & editing, Supervision. **S. George:** Formal analysis, Data curation. **D. Sedarsky:** Writing – review & editing, Supervision.

Declaration of competing interest

The authors declare that they have no known competing financial interests or personal relationships that could have appeared to influence the work reported in this paper.

Acknowledgments

This work was supported by the Swedish Energy Agency program for vehicle research and innovation (FFI), grant number 51459-1 and P2024-01000.

Data availability

Data will be made available on request.

References

[1] J. Buberger, A. Kersten, M. Kuder, R. Eckerle, T. Weyh, T. Thiringer, Total CO2-equivalent life-cycle emissions from commercially available passenger cars, Renew. Sustain. Energy Rev. 159 (2022) 112158.
[2] Y. Li, N. Ha, T. Li, Research on carbon emissions of electric vehicles throughout the life cycle assessment taking into vehicle weight and grid mix composition, Energies 12 (19) (2019) 3612.
[3] X. Hua, A. Thomas, K. Shultis, Recent progress in battery electric vehicle noise, vibration, and harshness, Sci. Prog. 104 (1) (2021) 00368504211005224.
[4] P. Bryła, S. Chatterjee, B. Ciabiada-Bryła, Consumer adoption of electric vehicles: A systematic literature review, Energies 16 (1) (2022) 205.
[5] J. Deng, C. Bae, A. Denlinger, T. Miller, Electric vehicles batteries: requirements and challenges, Joule 4 (3) (2020) 511–515.
[6] A. Ghasemi-Marzbali, et al., Fast-charging station for electric vehicles, challenges and issues: A comprehensive review, J. Energy Storage 49 (2022) 104136.
[7] T. Dimier, M. Cossale, T. Wellerdieck, Comparison of stator winding technologies for high-speed motors in electric propulsion systems, in: 2020 International Conference on Electrical Machines, ICEM, 1, IEEE, 2020, pp. 2406–2412.
[8] S.-W. Woo, J.-C. Park, M.-H. Sung, Y.-N. Bae, J. Yoon, K.-S. Cha, M.-S. Lim, Optimum design considering main operating points of EV traction motor for torque ripple reduction and fuel economy improvement, Int. J. Automot. Technol. 24 (1) (2023) 115–127.
[9] Z. Zhu, W. Chu, Y. Guan, Quantitative comparison of electromagnetic performance of electrical machines for HEVs/EVs, CES Trans. Electr. Mach. Syst. 1 (1) (2017) 37–47.
[10] Q. Chen, X. Fan, G. Liu, L. Xu, M. Xu, Regulation of high-efficiency region in permanent magnet machines according to a given driving cycle, IEEE Trans. Magn. 53 (11) (2017) 1–5.
[11] M. Ntombela, K. Musasa, K. Moloi, A comprehensive review for battery electric vehicles (BEV) drive circuits technology, operations, and challenges, World Electr. Veh. J. 14 (7) (2023) 195.
[12] U. Vollmer, U. Schäfer, An at-all operating points highly efficient PMSM for HEV, World Electr. Veh. J. 2 (4) (2008) 334–342.
[13] Z. Chen, P. Carvell, M. Younkins, Optimizing electric motor controls with dynamic motor drive, in: 30 Th Aachen Colloquium Sustainable Mobility, Aachen, 2021.
[14] M. Younkins, P. Carvell, J. Fuerst, Dynamic motor drive: Optimizing electric motor controls to improve efficiency, in: 42nd International Vienna Motor Symposium, 2021.
[15] M.Z. Islam, A. Singh, A. Arvanitis, M. Younkins, S. Leng, P. Carvell, A. Tripathi, Z. Chen, A. Phillips, Efficiency Improvement of Electric Motor Drives Using Dynamic Motor Drive Technology, Technical Report, SAE Technical Paper, 2022.
[16] M.Z. Islam, A. Phillips, S. Leng, B. Wolk, M. Younkins, P. Carvell, Reducing traction motor drive losses in electric vehicle using advanced torque modulation, in: 2023 IEEE International Electric Machines & Drives Conference, IEMDC, IEEE, 2023, pp. 1–7.
[17] R. Carter, A. Cruden, P.J. Hall, Optimizing for efficiency or battery life in a battery/supercapacitor electric vehicle, IEEE Trans. Veh. Technol. 61 (4) (2012) 1526–1533.
[18] J. Shen, S. Dusmez, A. Khaligh, Optimization of sizing and battery cycle life in battery/ultracapacitor hybrid energy storage systems for electric vehicle applications, IEEE Trans. Ind. Inform. 10 (4) (2014) 2112–2121.
[19] J. Břoušek, T. Zvolskỳ, Experimental study of electric vehicle gearbox efficiency, in: MATEC Web of Conferences, 234, EDP Sciences, 2018, p. 02004.
[20] M. Oh, I. Husain, Optimal torque distribution of dual-motor all-wheel drive electric vehicles for maximizing motor energy efficiency, in: 2021 IEEE Transportation Electrification Conference & Expo, ITEC, IEEE, 2021, pp. 188–193.
[21] Y. Xu, A. Kersten, S. Klacar, B. Ban, J. Hellsing, D. Sedarsky, Improved efficiency with adaptive front and rear axle independently driven powertrain and disconnect functionality, Transp. Eng. 13 (2023) 100192.
[22] C.T. Nguyen, B.-H. Nguyen, J.P.F. Trovao, M.C. Ta, Optimal drivetrain design methodology for enhancing dynamic and energy performances of dual-motor electric vehicles, Energy Convers. Manage. 252 (2022) 115054.
[23] Z. Wang, J. Zhou, G. Rizzoni, A review of architectures and control strategies of dual-motor coupling powertrain systems for battery electric vehicles, Renew. Sustain. Energy Rev. 162 (2022) 112455.
[24] EV reviews, *EV* tech specs, 2023, https://www.myevreview.com (Accessed 27 October 2023).
[25] C.T. Nguyen, B.-H. Nguyen, J.P.F. Trovão, M.C. Ta, Torque distribution optimization for a dual-motor electric vehicle using adaptive network-based fuzzy inference system, IEEE Trans. Energy Convers. (2023).
[26] C. Luo, Y. Yang, Z. Zhong, Optimal braking torque distribution of dual-motor front-rear individually driven electric-hydraulic hybrid powertrain based on minimal energy loss, IEEE Access 10 (2022) 134404–134416.
[27] J. Wang, S. Gao, K. Wang, Y. Wang, Q. Wang, Wheel torque distribution optimization of four-wheel independent-drive electric vehicle for energy efficient driving, Control Eng. Pract. 110 (2021) 104779.

[28] Q. Zheng, S. Tian, Q. Zhang, Optimal torque split strategy of dual-motor electric vehicle using adaptive nonlinear particle swarm optimization, Math. Probl. Eng. 2020 (2020) 1–21.
[29] X. Lai, S. Wang, S. Ma, J. Xie, Y. Zheng, Parameter sensitivity analysis and simplification of equivalent circuit model for the state of charge of lithium-ion batteries, Electrochim. Acta 330 (2020) 135239.
[30] S. Li, X. Cheng, A comparative study on RC models of lithium-ion battery, in: 2014 IEEE Conference and Expo Transportation Electrification Asia-Pacific (ITEC Asia-Pacific), IEEE, 2014, pp. 1–4.
[31] G. Lechner, H. Naunheimer, Automotive Transmissions: Fundamentals, Selection, Design and Application, Springer Science & Business Media, 1999.
[32] O. Theliander, A. Kersten, M. Kuder, W. Han, E.A. Grunditz, T. Thiringer, Battery modeling and parameter extraction for drive cycle loss evaluation of a modular battery system for vehicles based on a cascaded H-bridge multilevel inverter, IEEE Trans. Ind. Appl. 56 (6) (2020) 6968–6977, http://dx.doi.org/10.1109/TIA.2020.3026662.
[33] L. Harnefors, Control of power electronic converters and variable-speed drives, Västerås, Swed. Dep. Electron. Mälardalens Univ. (2002).
[34] H. Panagopoulos, K.J. Å ström, PID control design and H-infinity loop shaping, Int. J. Robust and Nonlinear Control IFAC-Affiliated J. 10 (15) (2000) 1249–1261.
[35] H. Fang, X. Duan, Y. Yang, Y. Wang, G. Luo, Deadbeat control of permanent magnet synchronous motor based on mras parameter identification, in: 2020 23rd International Conference on Electrical Machines and Systems, ICEMS, IEEE, 2020, pp. 161–166.
[36] J. Kennedy, R. Eberhart, Particle swarm optimization, in: Proceedings of ICNN'95-International Conference on Neural Networks, 4, ieee, 1995, pp. 1942–1948.
[37] E.A. Grunditz, T. Thiringer, Characterizing bev powertrain energy consumption, efficiency, and range during official and drive cycles from gothenburg, sweden, IEEE Trans. Veh. Technol. 65 (6) (2015) 3964–3980.
[38] P. Yu, T. Zhang, S. Chen, J. Li, R. Guo, Torsional Vibration Modeling of Driveline System for EV Low-Frequency Flutter, Technical Report, SAE Technical Paper, 2015.
[39] X. Hua, E. Gandee, Vibration and dynamics analysis of electric vehicle drivetrains, J. Low Freq. Noise Vib. Act. Control 40 (3) (2021) 1241–1251.
[40] S. Marco, W. Starkey, A concept of fatigue damage, Trans. Am. Soc. Mech. Eng. 76 (4) (1954) 627–632.
[41] D.L. Henry, A theory of fatigue-damage accumulation in steel, Trans. Am. Soc. Mech. Eng. 77 (6) (1955) 913–918.
[42] B. Bertsche, Reliability in Automotive and Mechanical Engineering: Determination of Component and System Reliability, Springer Science & Business Media, 2008.
[43] H. Dourra, Online driveline fatigue data acquisition method, SAE Int. J. Passeng. Cars-Electr. Electr. Syst. 6 (2013-01-1270) (2013) 301–306.
[44] S. Foulard, M. Ichchou, S. Rinderknecht, J. Perret-Liaudet, Online and real-time monitoring system for remaining service life estimation of automotive transmissions–Application to a manual transmission, Mechatronics 30 (2015) 140–157.
[45] C. Amzallag, J. Gerey, J.L. Robert, J. Bahuaud, Standardization of the rainflow counting method for fatigue analysis, Int. J. Fatigue 16 (4) (1994) 287–293.